Journal of Applied Electrochemistry (2022) 52:1353–1368
https://doi.org/10.1007/s10800-022-01717-7

RESEARCH ARTICLE

Boosted photoelectric cathodic protection exerted by 3D TiO_2/$AgInS_2$/In_2S_3 nanomultijunction for pure copper in NaCl solution

Mengmeng Sun[1,3,4] · Zhuoyuan Chen[2] · Xuhong Jiang[1,3,4,5] · Guiying Lu[1,3,4,5] · Jiangping Jing[2] · Chang Feng[2]

Received: 9 October 2021 / Accepted: 15 May 2022 / Published online: 2 June 2022
© The Author(s), under exclusive licence to Springer Nature B.V. 2022

Abstract

The global annual consumption of marine metal corrosion is a significant challenge to the service life of metals and the development of marine strategies. A tri-dimensional $AgInS_2$/In_2S_3 co-modified TiO_2 nanobush (NB) superstructure photoanode is constructed. It shows superior photoelectric cathodic protection (PECP) characteristic for pure copper whose self-corrosion potential is more negative in simulated natural marine environment without additional any hole scavengers under simulated solar light illumination. Origin from the more negative energy level potential of $AgInS_2$/In_2S_3, the quasi-Fermi level of the photogenerated electrons of TiO_2 NB/$AgInS_2$/In_2S_3 was pull to a more negative position, reinforcing the transmission of photogenerated electrons to the pure copper whose self-corrosion potential is more negative. The sensitizer $AgInS_2$ together with the assistant layer In_2S_3 dramatically enhances the PECP performance of TiO_2 NB/$AgInS_2$/In_2S_3. The tri-dimensional ultrafine branch-like architecture of TiO_2 NB with the nanoparticles quickens the collection and transfer of photogenerated electrons to the metallic pure copper. This environmentally friendly 3D photoanode structure provides a good reference for the optimized construction of photoelectric materials for marine metal corrosion protection.

Graphical abstract

The tri-dimensional $AgInS_2$/In_2S_3 co-modified TiO_2 nanobush superstructure photoanode possesses superior photoelectric cathodic protection characteristic for pure cooper whose self-corrosion potential is more negative in simulated marine environment under simulated solar light illumination.

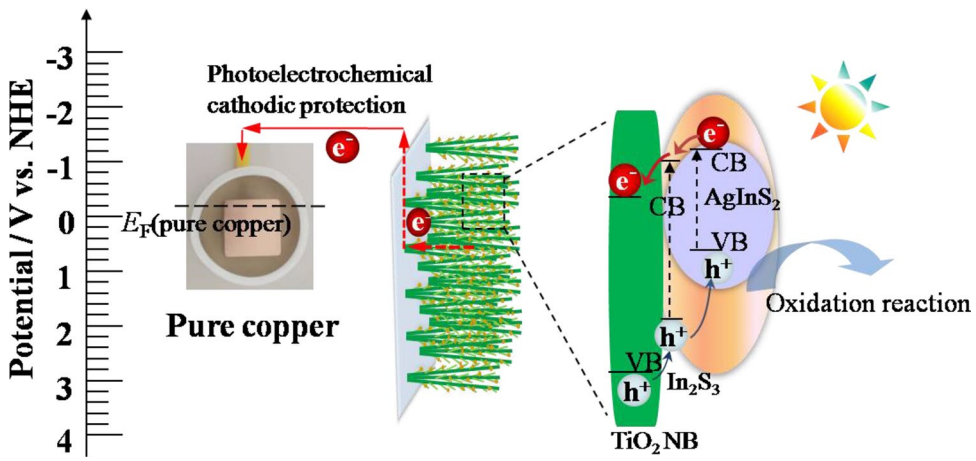

Keywords TiO_2 nanobush photoanode · 3D nanomultijunction · Photoelectric cathodic protection · NaCl solution

✉ Zhuoyuan Chen
zychen@fosu.edu.cn

Extended author information available on the last page of the article

1 Introduction

Due to the harsh marine environment, marine environmental corrosion of metal materials is a huge challenge faced by many marine engineering materials. To overcome this challenge, research on various corrosion protection technologies are stepped up to develop high efficient corrosion protection methods for providing a better corrosion protection against corrosion failure. Solar radiation energy is very rich in marine environment. With the current rapid development of photoelectrochemical technology in various fields, a cutting-edge corrosion protection technology-photoelectric cathodic protection (PECP) technology has been attracting more and more interests [1–5]. This PECP technology use semiconductor materials to absorb and converse solar radiation to electrons and realize the application of photogenerated electrons for the cathodic protection of metals. With the optimization of the nano-multiphase junction structure, the photoelectric conversion performance has been gradually improved, and the application of photoelectric conversion technology has been constantly promoted [6–8]. Many various methods, such as the single doping, dual doping and multi-element co-doping, the metal/metal oxide/metal sulfide deposition, as well as the co-modification with multiple ways, are all being investigated for optimizing the photoelectrochemical materials, so as to improve the application performance of photoelectric conversion in various fields [9–20]. Therefore, it is urgent to boost the PECP performance to promote the practical application of PECP in marine environment for metals with negative self-corrosion potentials.

Compared with the two-phase junction, the multi-phase junction will be able to promote the electron transmission more efficiently. Multiple semiconductor junctions built in a structure will promote the photoelectrochemical conversion performance. Constructing a multi-phase junction structure with energy band gradient matching in a photoelectric semiconductor thin film material will boost the photoelectric conversion performance. Dong et al. proved that three-component nanojunction system will enhance the visible light PEC conversion activity, and the band structure over the three-component nanojunction system plays an important role for the improvement of its PEC conversion activity [21]. The three-component nanojunction photocatalyst system exhibited six times higher visible-light activity than that of the pristine C-doped TiO_2 in the degradation of toluene in air [21]. Liu et al. proved that CoO/CdS/TiO_2 photocatalyst showed higher efficiency in the photocatalytic degradation [22]. The multijunction is also popular applied in solar cell, which can offer matched structure and provide a desirable bandgap [23]. So, bandgap engineered architectures for high-efficiency multijunction solar cells are research hotspots in the field of solar cell. And optimization of the photoanode is required to maximize light absorption and minimize the transfer barrier in the semiconductor system. So, constructing multijunction with matched band structure is an effective method for attaining high-efficiency photoelectric conversion performance. King et al. reported that metamorphic three-junction GaInP/GaInAs/Ge solar cell under the simulated solar spectrum shows high solar conversion efficiency of 40% [24]. Layer by layer matching band structure is very conducive to the performance of solar cells. Finally, multijunction can alleviate the problems associated with the unmatched band structure and offers further improvements [24].

Besides, for designing multijunction nanoarchitecture photoanode, the ultrafine structure is also crucial for greatly reducing the migration resistance and transfer barrier, improving the transfer and collecting of photoinduced electrons, and decreasing the electron–hole recombination. Simultaneously, the ultrafine structure can maximize the light capture area, and the quantum size effect brought by the ultrafine structure will also benefit the improvement of photoelectric conversion performance. Dai et al. also confirmed that the PEC performance of the nanocomposite is closely correlated to the size for the α-Fe_2O_3 nanocrystals, and small nanocrystals display better PEC properties [25]. The ultrafine cobalt iron oxide nanoparticle can promote the charge separation and show high performance in photoelectrochemical water oxidation [26]. Wang et al. reported that ultrafine hematite α-Fe_2O_3 nanowire array electrode has higher photocurrent and charge separation efficiency than nanorod electrode [27]. So, ultrafine structure is also important for developing potential photoanodes for enhancing the PECP performance.

In this paper, we combine multijunction with ultrafine structure for boosting the PEC and PECP performance. A TiO_2/$AgInS_2$/In_2S_3 nanobush (NB) photoanode was constructed, and it shows highly efficient PECP performance for pure copper in 3.5 wt% NaCl solution (similar to marine environment) under the simulated solar light illumination. The gradient matched energy level and ultrafine charge transmission pathway within the ultrafine multijunctions together promote the separation of photogenerated electron–hole pairs, and then leads to the markedly enhanced PEC and PECP performances in the simulated marine environment. This work provides a new insight into the design of photoanode for the application of PECP in marine metal corrosion protection.

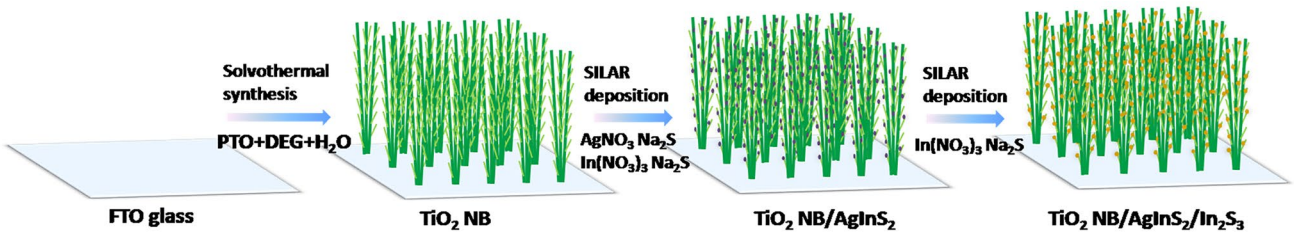

Scheme 1 The fabrication procedure of the TiO_2 NB/$AgInS_2$/In_2S_3 photoanode

2 Experimental

2.1 Synthesis of TiO_2 NB and modified TiO_2 NB film

The ultrafine branched TiO_2 NB substrate was prepared on FTO conductive glass by a facile one-step solvothermal and then calcination method reported in our recent work [28], the detailed preparation process is described below. 0.002 mol potassium titanium oxalate ($K_2TiO(C_2O_4)_2$) was dissolved in 10 mL deionized water and 30 mL diethylene glycol (DEG), and stirred for 30 min. The FTO conductive glass was placed into the Teflon-lined stainless-steel autoclave at an angle to the inner wall of the Teflon-liner, and the conductive surface is downward. Then, the above mixed solution was poured into the Teflon-liner. Then the solvothermal reaction was carried out at 180 °C for 9 h. After solvothermal reaction, the FTO conductive glass was taken out after the autoclave was cooled, and rinsed with deionized water and dried. Finally, the FTO conductive glass was calcined in a tube furnace at 450 °C for 1 h in the air to get the TiO_2 NB.

The fabrication of TiO_2 NB/$AgInS_2$/In_2S_3 film photoanode is illustrated in Scheme 1 which is described as follows. Decorate $AgInS_2$ on the TiO_2 NB by a successive ion layer absorption and reaction (SILAR) technique. First, immerse the synthesized TiO_2 NB film in the solution of 0.01 M $AgNO_3$ under ambient condition. After impregnating for 4 min, the sample was washed with purified water. Then immerse the TiO_2 NB film in the solution of 0.01 M Na_2S for 4 min and washed with purified water. Then, immerse the TiO_2 NB film in the solution of 0.01 M $In(NO_3)_3$ for 4 min and washed with purified water; afterwards immerse the TiO_2 NB film in the solution of a 0.01 M Na_2S aqueous solution for 4 min and washed with purified water. This process is a cycle of depositing silver indium sulfide, and repeat this deposition cycle for several times to adjust the quantity of $AgInS_2$ on the TiO_2 NB film [29, 30].

Next step, the TiO_2 NB/$AgInS_2$ film was further decorated with the In_2S_3 assistance layer via SILAR deposition. The deposition process of In_2S_3 is the same to the deposition process of $AgInS_2$ without immersing in the solution of $AgNO_3$, and adjusting the number of deposition cycles to control the amount of In_2S_3. The prepared photoanode was named TiO_2 NB/$AgInS_2$(a)/In_2S_3(b), where a and b are representatives of the number of deposition cycles for $AgInS_2$ and In_2S_3, respectively. For comparison, the corresponding $AgInS_2$ and In_2S_3 powder was also synthesized by dropping the Na_2S solution to the $AgNO_3 + In(NO_3)_3$ or $In(NO_3)_3$ solutions as described in our previous report [31].

Prepare the metal electrode by encapsulating a cubic copper block of 1 cm^3 in epoxy resin. The exposed surface of 1 cm^2 was used to test the corrosion electrochemical performance of the metal surface. Then the pure copper electrode was polished, cleaned, dried and then stored in a desiccator for later use.

2.2 Characterizations

The morphologies of the samples were characterized on a scanning electron microscope (SEM) (Hitachi cold field emission SU8220) and a high resolution transmission electron microscope (HRTEM, Tecnai G20, FEI Company, USA). The crystalline structures were measured on X-ray diffractometer (XRD). In order to characterize the changes in the surface composition of the composite, the X-ray photoelectron spectroscopies (XPS) of the samples were characterized on ESCALAB 250Xi (Thermo Fisher Scientific Inc.; Mono X-ray source, Al Kα radiation; binding energy calibrated according to C1s = 284.8 eV). The photoabsorption performances were detected on the UV–Vis diffuse reflectance absorption spectra (SHIMADZU UV-2600, Japan).

2.3 PEC and electrochemical characterizations

PEC characterizations were carried out on a CHI 660E electrochemical work station (Shanghai Chenhua Instrument Co., Ltd.) with a three-electrode system. A Ag/AgCl (saturated KCl) and a Pt electrodes were used as reference electrode and counter electrode, respectively. The prepared photoanodes were used as the work electrode. The exposed area was 1 cm^2. In order to approach the real marine environment to a great extent, 3.5 wt% NaCl solution without adding any hole scavengers was used as the electrolyte. The PEC test device cell used here is the same as that used in our previous work [32]. The light source was a 300 W PLS-SXE300

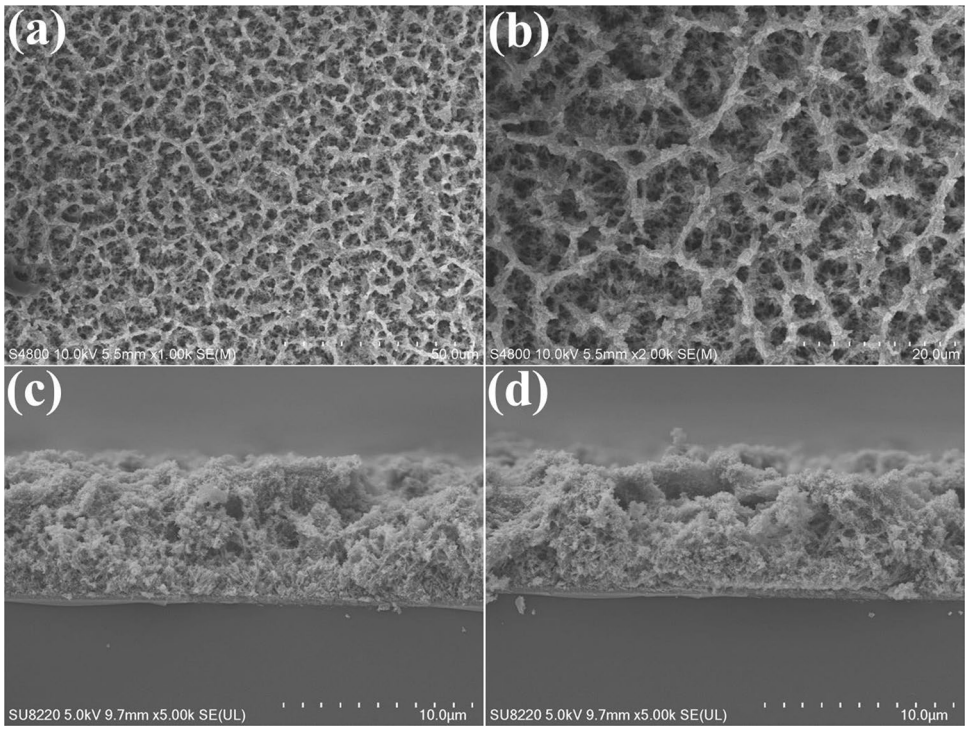

Fig. 1 The SEM top-view images (**a**, **b**) and cross-sectional images (**c**, **d**) of TiO_2 NB/$AgInS_2(3)/In_2S_3(7)$

Xe arc lamp (Beijing PerfectLight Co. Ltd., China) with an AM1.5 filter to get the simulated solar light illumination. The light density was 100 mW cm^{-2}. Under this simulated marine environment (3.5 wt% NaCl solution), the photoinduced i-V curves of the prepared photoanodes were measured with a scan rate of 0.01 V s^{-1} under light cutting on and off. For identifying the variation of the charge carriers transfer capability of the film photoanode after modification, the resistances of the prepared film photoanodes were measured through the electrochemical impedance spectroscopy (EIS) conducted in 3.5 wt% NaCl solution in the dark at open circuit potential over frequency range from 10^5 to 10^{-2} Hz with a 5 mV AC amplitude. The Mott–Schottky plots of the prepared film photoanodes were measured in 0.1 Na_2SO_4 solution in the dark. Besides, in order to measure the separation efficiency of photogenerated electron and hole of the prepared photoanode, test the photoluminescence (PL) emission intensity of the synthesized samples on a fluorescence spectrometer (Fluoro Max-4, HORIBA Jobin Yvon, France).

2.4 PECP tests

The PECP properties of the synthesized photoanodes were performed using the device cell previously used in our work [32]. Using CHI 660E electrochemical workstation, the photoinduced variations of the mixed potentials of the coupling of the photoanode and the metal electrode were measured; and the photoinduced cathodic protection current densities of the prepared photoanode for the coupled pure copper electrode were measured. Also, the 3.5 wt% NaCl solution without additional hole scavengers was used in this measurement. The light source was the same to that used above.

3 Results and discussion

3.1 Structural characteristics of the fabricated $AgInS_2/In_2S_3$ decorated TiO_2 NB

The microscopic structure of the fabricated TiO_2 NB/$AgInS_2(3)/In_2S_3(7)$ were characterized by SEM. Figure 1a–d show the SEM top-view images (a, b) and cross-sectional images (c, d) of TiO_2 NB/$AgInS_2(3)/In_2S_3(7)$ in a wide scope, from which a loose porous nanobush-like structure can be seen. Figure 2a–d show the SEM top-view images with progressive magnification, from which the porous structure composed of many branchlets compactly packed together can be observed similar to the fabricated pure TiO_2 NB shown in our resent work [33]. From the magnified SEM image (Fig. 2d), it can be seen that the TiO_2 NB is deposited with a large number of nanoparticles (NPs). The NPs distributed uniformly on the nanobranchlets. The large amount of NPs forms well interfacial adhesion with the TiO_2 NB. Owing to the ultrafine nanobranchlets, the deposited NPs on them were also refined. This 3D ultrafine multijunction architecture ensures the sufficient harvesting and utilization of light. Figure 3a, b show the cross-sectional SEM images of the TiO_2 NB/$AgInS_2(3)/In_2S_3(7)$ photoanode, numerous

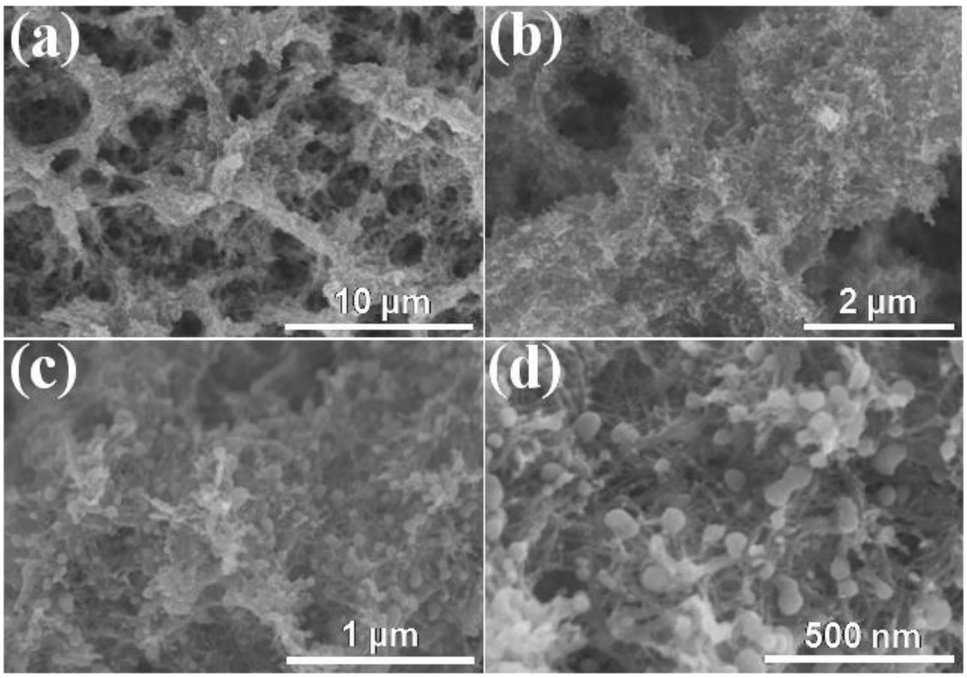

Fig. 2 The SEM top-view images of TiO_2 NB/$AgInS_2$(3)/In_2S_3(7) with progressive magnification

nanobranchlets of the TiO_2 NB grew on the FTO glass, with the film thickness of approximately 7.3 μm. A larger number of deposited NPs are distributed both inside and on the upper surface of the TiO_2 NB layer. In order to reveal the elemental distribution on the TiO_2 NB/$AgInS_2$(3)/In_2S_3(7) photoanode, the EDS elemental mapping images corresponding to the framed area of the cross-sectional SEM image in Fig. 3a were given. The results reveal a uniform distribution of Ag, In and S elements on TiO_2 NB. These analyses reveal that the NPs are sufficiently deposited and adhered onto the TiO_2 NB architecture through the SILAR technique, forming multijunction photoanode. For TiO_2 NB/$AgInS_2$(3)/In_2S_3(7), the ultrafine multijunction architecture will also ensure the harvesting of visible light through the $AgInS_2$/In_2S_3.

The TiO_2 NB/$AgInS_2$(3), TiO_2 NB/$AgInS_2$(3)/In_2S_3(7) as well as TiO_2 NB/In_2S_3(14) samples were further characterized using TEM and HRTEM, and the results are shown in Figs. 4 and 5. Figure 4a, a1, b display the TEM and HRTEM images of TiO_2 NB/$AgInS_2$(3), and Fig. 4a1 is the magnified image of the framed area in Fig. 4a, in which shows the branchlets in bundles. The diameter of the branchlets is approximately 10 nm, and numerous NPs adhered on them are in size of 10 nm. The HRTEM image of TiO_2 NB/$AgInS_2$(3) (Fig. 4b) displays lattice spacings of 0.267 nm and 0.352 nm matched with the (110) and (101) planes of TiO_2 anatase [34, 35], verifying the anatase crystallite of TiO_2. And the lattice spacing of 0.312 nm for the NPs on the nanobranchlets matches with the (121) plane of orthorhombic $AgInS_2$ [35, 36].

Figure 4c, c1 display the TEM images of TiO_2 NB/$AgInS_2$(3)/In_2S_3(7), Fig. 4c1 is the magnified image of the framed area in Fig. 4c. The morphology is similar with those in Fig. 4a, a1. Figure 4d displays the HRTEM image of TiO_2 NB/$AgInS_2$(3)/In_2S_3(7), the lattice fringes of 0.267 nm and 0.352 nm match with the interplanar spacings of the (110) and (101) planes of anatase, the lattice fringe of 0.242 nm of the NPs on the nanobranchlets corresponds to the interplanar spacing of the (122) plane of orthorhombic $AgInS_2$ [37]. The phase in weak crystallinity around the $AgInS_2$ NPs in Fig. 4d might be the In_2S_3 phase. In order to confirm the state of In_2S_3 in the sample, the In_2S_3 was largely deposited onto the TiO_2 NB with 14 cycles, and the corresponding TEM and HRTEM images of TiO_2 NB/In_2S_3(14) are shown in Fig. 5. Figure 5a, a1, c, c1 are the TEM images, and Fig. 5a1 and c1 are the magnified images of the framed area in Fig. 5a and c, respectively. For TiO_2 NB/In_2S_3(14), a layer is wrapped compactly on the TiO_2 branchlets. Figure 5b, d are the corresponding HRTEM images, the lattice fringes of 0.32 nm on the nanobranchlets corresponds to an interplanar spacing of the (109) plane of tetragonal β-In_2S_3 phase [38, 39]. These results confirm that the In_2S_3 constructed by SILAR technique wrapped onto the TiO_2 NB is in form of layer. So, for TiO_2 NB/$AgInS_2$(3)/In_2S_3(7) photoanode, the In_2S_3 layer is wrapped onto the $AgInS_2$ NPs sensitized TiO_2 NB as a assistance layer. Then, the TiO_2 NB/$AgInS_2$(3)/In_2S_3(7) tri-phase junction was successfully constructed. Compared with bi-phase junction of TiO_2 NB/$AgInS_2$(3) and TiO_2 NB/In_2S_3(7), the TiO_2 NB/$AgInS_2$(3)/In_2S_3(7) tri-phase junction constructed with gradient matched energy level will further accelerate the separation and transmission of the photoinduced electron

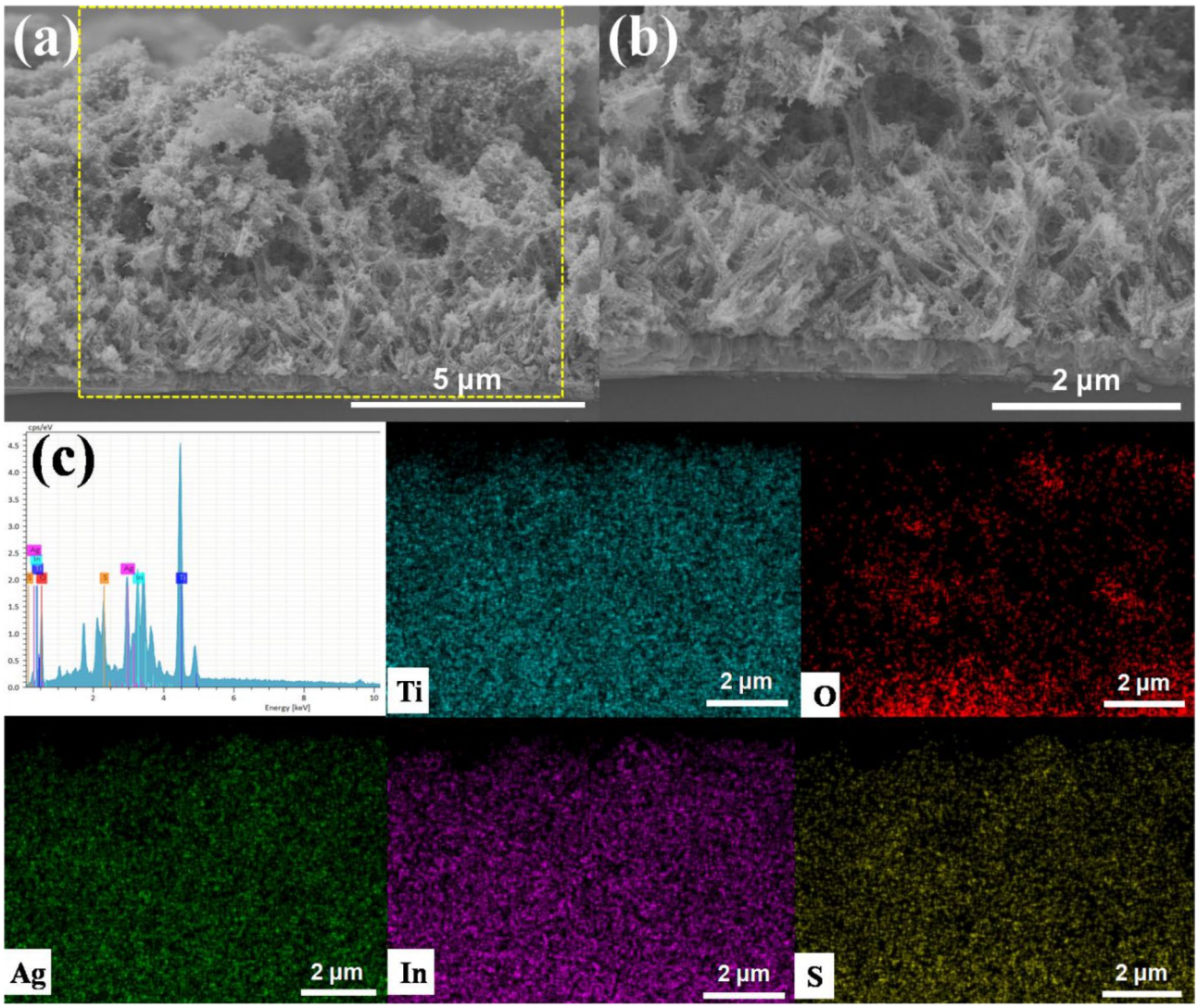

Fig. 3 SEM cross-sectional images (**a**, **b**) and the corresponding EDS elemental mapping results (**c**) of the frame area in **a** of the TiO_2 NB/$AgInS_2$(3)/In_2S_3(7) photoanode

and hole in the photoanode. And the ultrafine TiO_2 NB substrate will greatly reduce the electron transmission barrier to transport photogenerated electrons efficiently.

The crystalline phases of the fabricated $AgInS_2$/In_2S_3, $AgInS_2$, In_2S_3 decorated TiO_2 NB and plain TiO_2 NB were characterized by XRD patterns as shown in Fig. 6. The diffraction peaks matched with TiO_2 (PDF#21-1272) and FTO glass are clearly seen. Besides, for TiO_2 NB/$AgInS_2$(3)/In_2S_3(7) and TiO_2 NB/$AgInS_2$(3), the diffraction peaks at 26.7°, 29.0°, 31.7°, 34.5°, 36.9° are ascribed to the $AgInS_2$ phase (PDF#25-1328) [29]. For TiO_2 NB/In_2S_3(7), the diffraction peaks at 32.6° may be caused by the deposited In_2S_3. No evident diffraction peaks of In_2S_3 can be detected for the TiO_2 NB/$AgInS_2$(3)/In_2S_3(7) or TiO_2 NB/In_2S_3(7), due to the fewer amount of In_2S_3 on these samples and the lower crystallinity of the In_2S_3 synthesized via SILAR technique.

XPS analyses were carried out to confirm the chemical states of the components in TiO_2 NB/$AgInS_2$(3)/In_2S_3(7). Figure 7 shows the high-resolution XPS spectra of Ti 2p, O 1s, In 3d, Ag 3d and S 2p. In Fig. 7a, the binding energy peaks at 458.2 and 464 eV are assigned to Ti $2p_{3/2}$ and Ti $2p_{1/2}$, the binding energy peaks at 445.1 and 452.7 eV are assigned to In $3d_{5/2}$ and In $3d_{3/2}$ [36], revealing the oxidation state of In is + 3. The positive shift of the binding energies of Ti $2p_{3/2}$ and Ti $2p_{1/2}$ peaks of TiO_2 NB/$AgInS_2$(3), TiO_2 NB/$AgInS_2$(3)/In_2S_3(7), TiO_2 NB/In_2S_3(7) compared to those of TiO_2 NB is due to the strong electron attracting effect of $AgInS_2$ and In_2S_3. Because the electronegativity of Ag^+, In^{3+}, S^{2-} are larger than that of Ti^{4+}, the Ag^+, In^{3+}, S^{2-} possess strong electron-withdrawing effect on Ti^{4+},

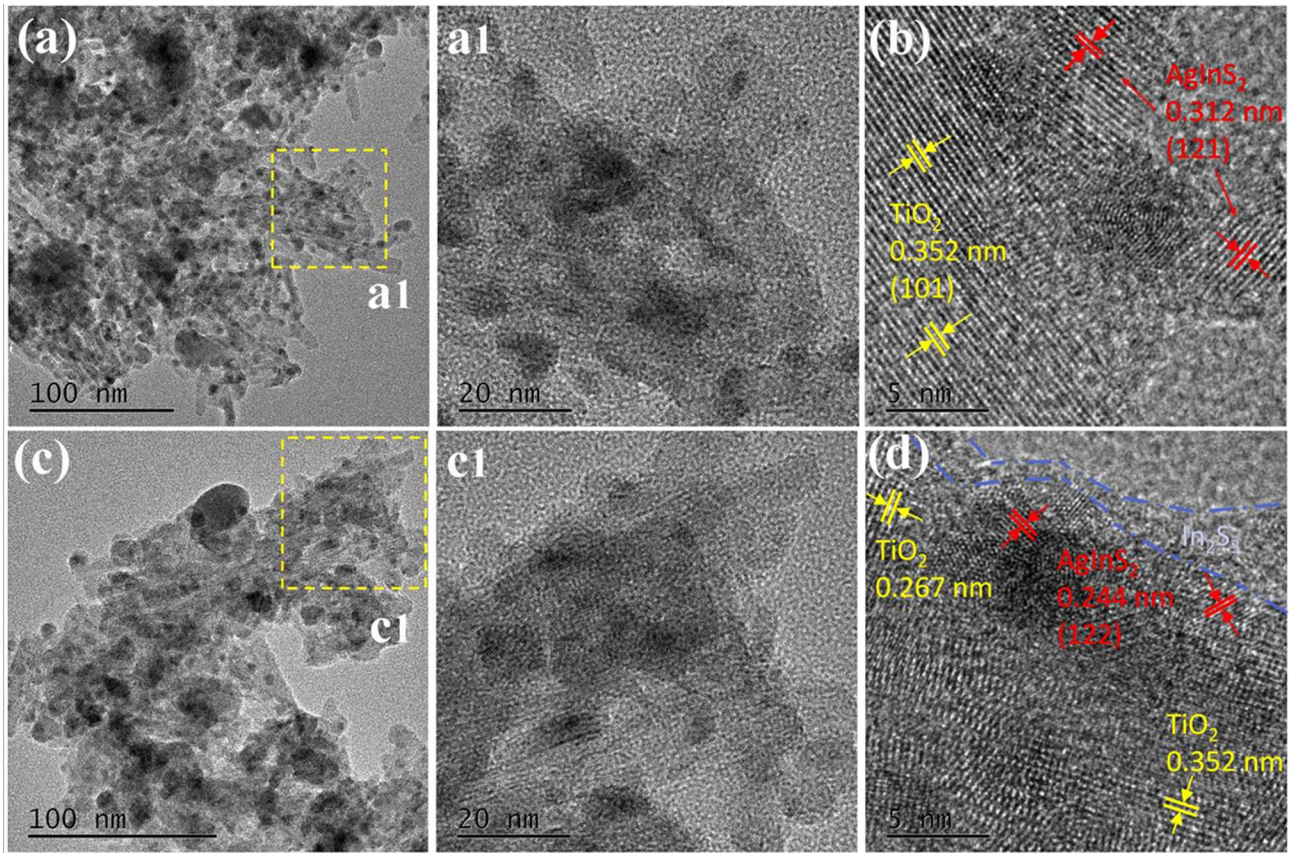

Fig. 4 TEM and HRTEM images of the microstructures of the prepared TiO_2 NB/$AgInS_2$(3) (**a**, **a1**, **b**) and TiO_2 NB/$AgInS_2$(3)/In_2S_3(7) (**c**, **c1**, **d**)

inducing the electron density around Ti^{4+} lower than that without compounding. Then the Ti^{4+} nucleus will exert a stronger electron binding ability for outer electrons, resulting in the positive shift of the binding energies of Ti^{4+} towards high binding energy. Besides, the intensities of the binding energy peaks of In 3d are gradually increased for TiO_2 NB/$AgInS_2$(3), TiO_2 NB/$AgInS_2$(3)/In_2S_3(7), TiO_2 NB/In_2S_3(7) compared with those of pure TiO_2 NB, indicating the successful deposition of $AgInS_2$ and In_2S_3. And the intensity of the binding energy peaks of Ti 2p is gradually decreased for TiO_2 NB/$AgInS_2$(3)/In_2S_3(7) and TiO_2 NB/In_2S_3(7), confirming that the deposition of In_2S_3 is in the form of layer rather than nanoparticles on the surface of TiO_2 NB, then blocking the binding energy signal of TiO_2 substrate.

In Fig. 7b, the peaks at 529.5 and 531.6 eV are assigned to lattice oxygen (O_L) and adsorbed oxygen (O_A). Similar shift of the binding energy peaks of O_L and O_A for TiO_2 NB/$AgInS_2$(3), TiO_2 NB/$AgInS_2$(3)/In_2S_3(7), TiO_2 NB/In_2S_3(7) towards the direction of high binding energy can be seen, as compared to those of single TiO_2 NB. Because S^{2-} has a strong ability to attract electrons towards S atom in the compound, the electron density around O is lower than before compounding. The binding ability of O element nuclei is strengthened to bind extranuclear electrons, leading to the shifts of the binding energy peaks of O towards high binding energy. A similar phenomenon was also reported by other literatures [40], which is caused by the sulfide deposition, resulting in the influence on the electron-withdrawing interaction among the elements in the prepared composite, thus resulting in the shift of binding energy peak in XPS spectra [41–43]. Besides, the binding energy peak of O_A reveals the existence of adsorbed water molecules or hydroxyl groups on the surface of the composite [33]. The increase in the intensity of the binding energy peak of O_A for TiO_2 NB/$AgInS_2$(3), TiO_2 NB/$AgInS_2$(3)/In_2S_3(7), TiO_2 NB/In_2S_3(7) compared with those of TiO_2 NB reveals the increase in the surface adsorption characteristic.

In Fig. 7c, the high-resolution XPS spectra of Ag 3d, the two peaks at 368.1 and 374 eV are assigned to Ag $3d_{5/2}$ and Ag $3d_{3/2}$ [44], respectively, indicating that the oxidation states of Ag is + 1. The position of the binding energy peak of Ag in TiO_2 NB/$AgInS_2$(3) is higher than that in TiO_2 NB/$AgInS_2$(3)/In_2S_3(7). It is related with the lower electronegativity of In (1.78) compared with that of Ag (1.93). So, after further deposition of In_2S_3(7) layer on TiO_2 NB/$AgInS_2$(3), the binding energy peaks of Ag shift slightly

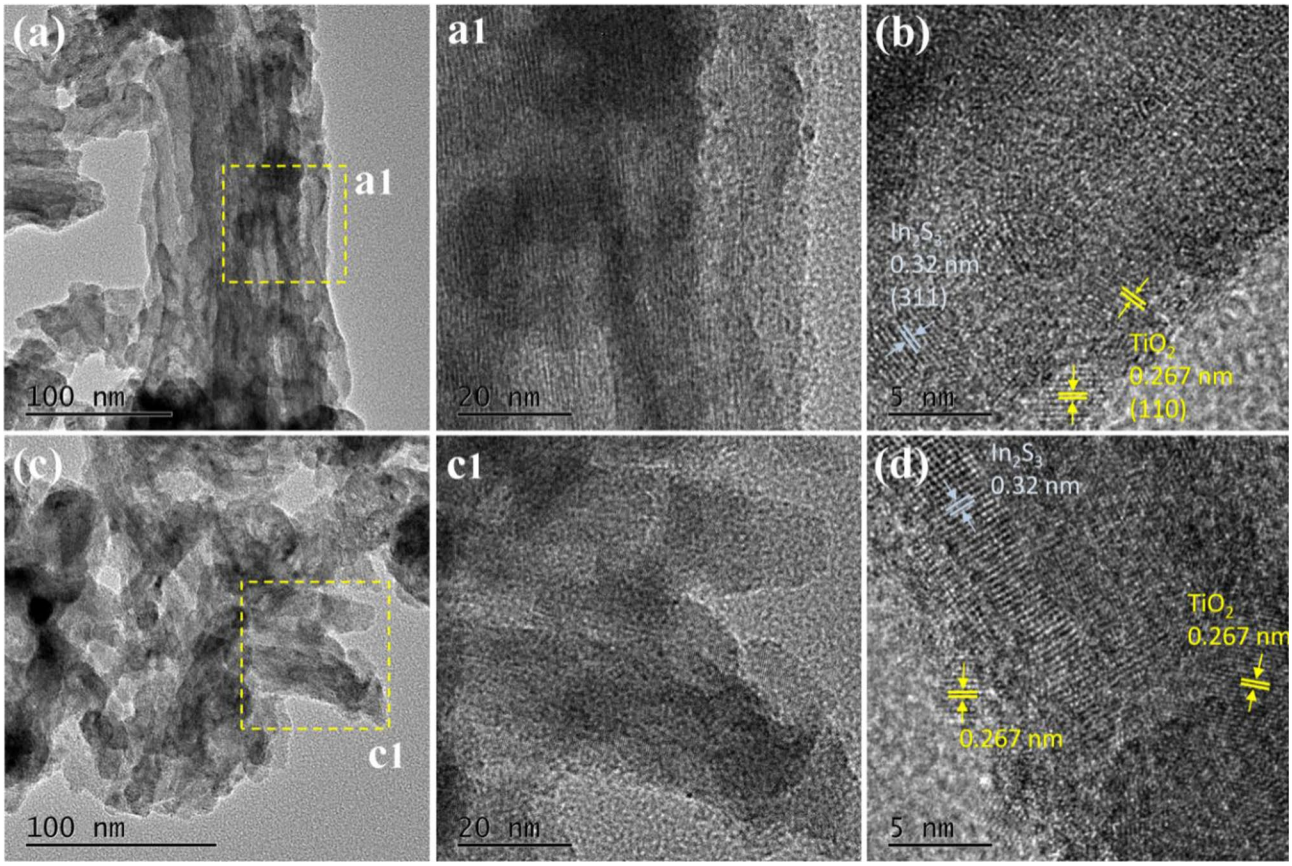

Fig. 5 TEM **a**, **a1**, **c**, **c1** and HRTEM **b**, **d** images to show the detail microstructure information of TiO2 NB/In2S3(14). **a1**, **c1** are the further enlarged images of the framed areas in Fig. (a), (c) respectively

towards lower binding energy. This result is also in consistent with the results in Fig. 6a and b in which the TiO_2 NB/$AgInS_2$(3) shows the highest binding energy peak positions of In, Ti and O.

Figure 7d shows the S 2p XPS core level spectra, the broad asymmetric binding energy peaks at 161.1 and 162.3 eV for TiO_2 NB/$AgInS_2$(3) are assigned to the S $2p_{3/2}$ and S $2p_{1/2}$ of S^{2-} in $AgInS_2$, and the broad asymmetric binding energy peaks at 161.8 and 163.2 eV for TiO_2 NB/In_2S_3(7) are assigned to the S $2p_{3/2}$ and S $2p_{1/2}$ of S^{2-} in In_2S_3 [36, 45]. The binding energy peak position of TiO_2 NB/$AgInS_2$(3)/In_2S_3(7) covers the peak positions of S^{2-} in $AgInS_2$ and S^{2-} in In_2S_3 [31, 46]. These results verify that both $AgInS_2$ and In_2S_3 have been decorated onto TiO_2 NB. The above HRTEM and XPS results validate that the decorated $AgInS_2$ and In_2S_3 on TiO_2 NB forms close interfacial combination with the TiO_2 NB substrate.

3.2 UV–Vis absorption and PEC properties of the film photoanodes

The optical absorption activities of TiO_2 NB/$AgInS_2$(3), TiO_2 NB/$AgInS_2$(3)/In_2S_3(7), TiO_2 NB/In_2S_3(7), TiO_2 NB and the corresponding $AgInS_2$ and In_2S_3 powder were measured by UV–Vis absorption spectra as shown in Fig. 8a. The UV–Vis optical absorption region of the single TiO_2 NB is at 200–382 nm, corresponding to its UV light responsive property with the bandgap of 3.2 eV. The $AgInS_2$ powder with black brown color shows a much wider optical absorption, which is due to its bandgaps of 1.83–1.92 eV, that is consistent with the optical absorption properties described in other literatures [47–49]. And the optical absorption threshold of the $AgInS_2$ powder is at 614 nm deduced to the bandgap of 2 eV, which is close to the values reported previously [47–49]. The In_2S_3 powder with light yellow color exhibits optical absorbing in the UV–Vis region of 200–470 nm. And the optical absorption threshold of the In_2S_3 powder is at 455 nm deduced to the bandgap of 2.7 eV. For TiO_2 NB/$AgInS_2$(3) and TiO_2 NB/$AgInS_2$(3)/In_2S_3(7), the absorbance of the UV–Vis absorption spectra in the region of

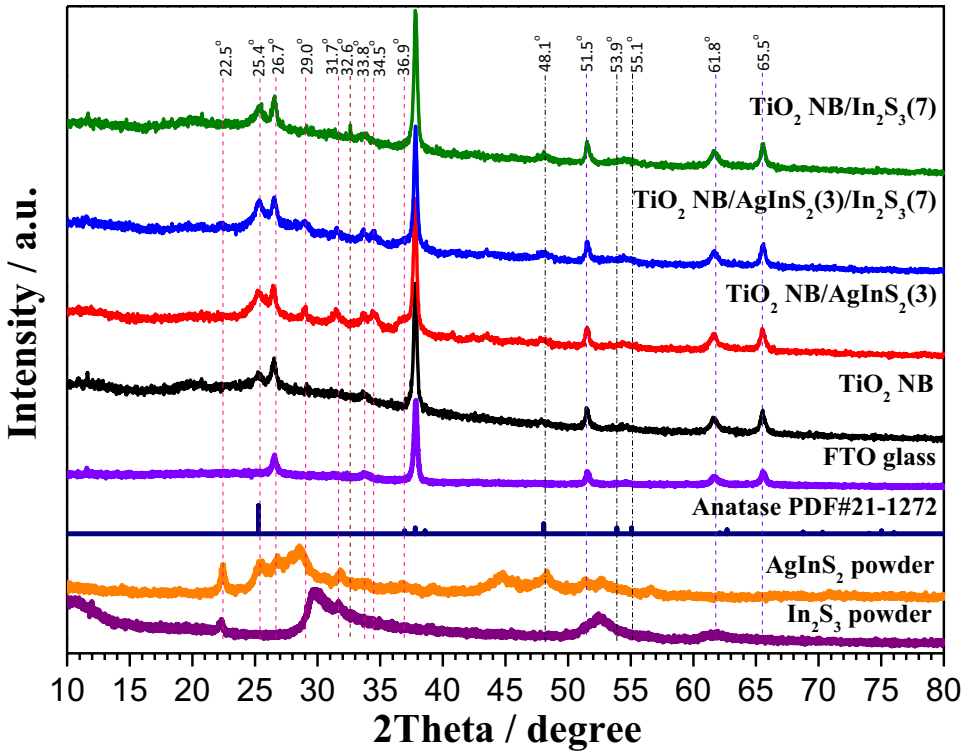

Fig. 6 XRD patterns of the prepared photoanodes and samples

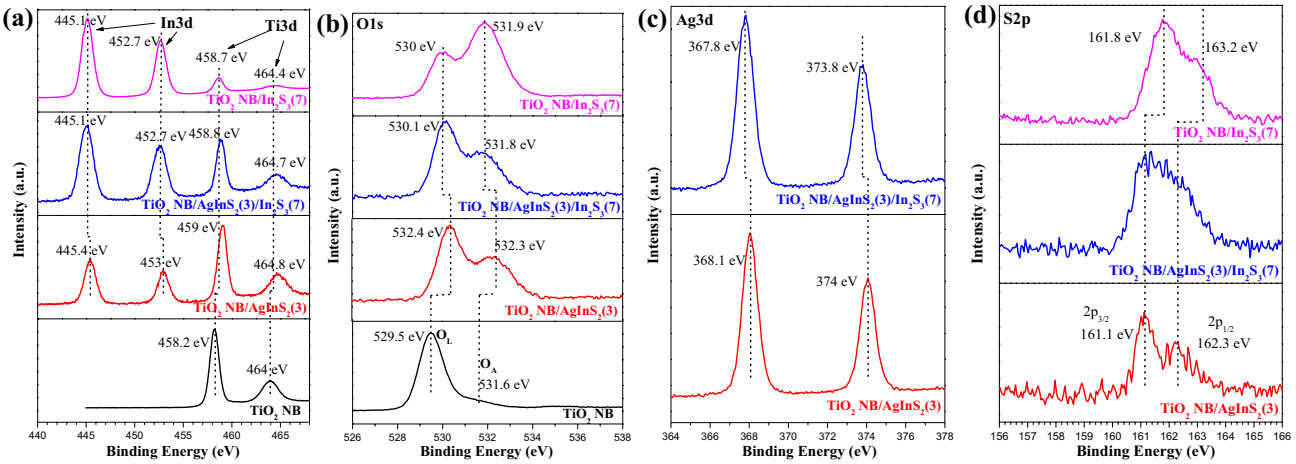

Fig. 7 XPS spectra of (**a**) In 3d and Ti 3d, (**b**) O 1s, (**c**) Ag 3d, and (**d**) S 2p of the prepared photoanodes

340–800 nm dramatically enhances compared with those of pure TiO_2 NB, which is ascribed to the brown $AgInS_2$ NPs decoration over the TiO_2 NB surface. The TiO_2 NB/$AgInS_2(3)/In_2S_3(7)$ photoanode exhibits a optimal absorption property both in the visible light region and UV light region due to the sensitization of the $AgInS_2(3)/In_2S_3(7)$. For TiO_2 NB/$In_2S_3(7)$, the absorbance only enhances slightly compared to that of TiO_2 NB, which is caused by the very few deposited In_2S_3 layer, only slightly affects the optical absorption property of TiO_2 NB. Finally, the TiO_2 NB/$AgInS_2(3)/In_2S_3(7)$ photoanode with the optimal optical absorption ability will help to achieve the highly efficient PEC conversion performance during applications under simulated solar light irradiation.

Figure 8b shows the photoinduced i-V curves of the TiO_2 NB/$AgInS_2(3)$, TiO_2 NB/$AgInS_2(3)/In_2S_3(7)$, TiO_2 NB/$In_2S_3(7)$, TiO_2 NB photoanodes under switching on and off the simulated solar light illumination in the NaCl solution. The pure TiO_2 NB exhibits much smaller photoinduced current (only approximately 3.8 μA cm^{-2} under the bias of 0 V

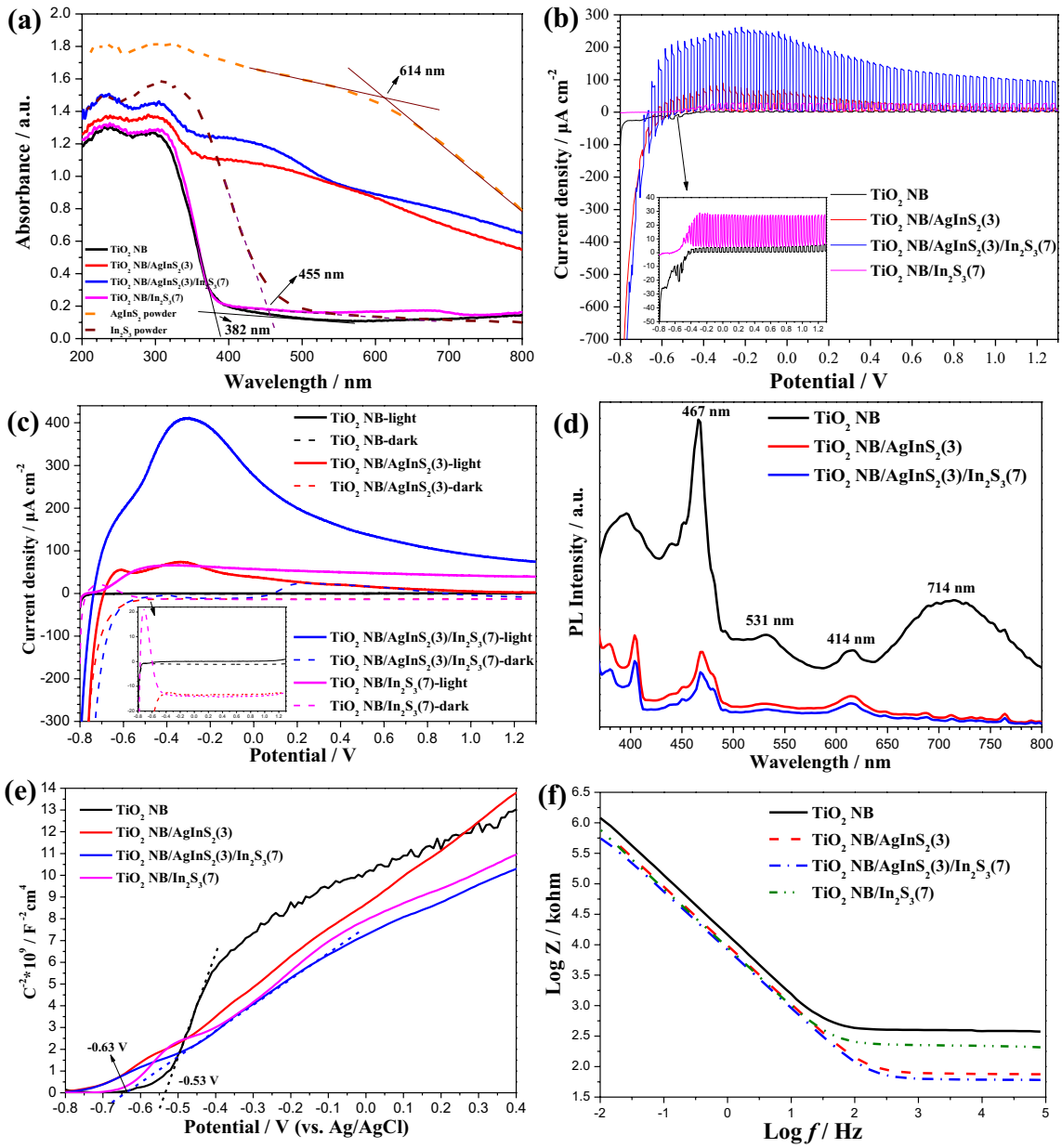

Fig. 8 The UV–Vis absorption spectra (**a**), photoinduced i-V curves (**b**), i-V curves under AM1.5 light irradiation and in the dark (**c**), PL emission spectra (**d**), Mott–Schottky plots (**e**) and EIS Bode plots (**f**) of the prepared samples. The energy density of the light used in **b**, **c** is 100 mW cm^{-2}

vs. Ag/AgCl). After uniform deposition of $AgInS_2$ onto TiO_2 NB, its photoinduced current density increases to 57 μA cm^{-2} (under the bias of 0 V vs. Ag/AgCl) caused by the sensitization of $AgInS_2$ and the interfacial heterojunction effect of TiO_2/$AgInS_2$. And after only depositing the In_2S_3 layer onto TiO_2 NB, its photoinduced current density increases to 26 μA cm^{-2} (under bias of 0 V vs. Ag/AgCl). Importantly, it is noted that compared with TiO_2 NB/$AgInS_2$(3) and TiO_2 NB/In_2S_3(7), TiO_2 NB/$AgInS_2$(3)/In_2S_3(7) exhibits a further increased photoinduced current density with the value of around 230 μA cm^{-2} (under bias of 0 V vs. Ag/AgCl). For TiO_2 NB/$AgInS_2$(3)/In_2S_3(7), the deposited In_2S_3 layer around TiO_2 NB/$AgInS_2$(3) constructs a tri-phase junction, which possesses gradient matched energy level, further boosts the transmission of the photogenerated electron and hole through the interfaces of TiO_2/$AgInS_2$/In_2S_3, reducing recombination of photogenerated electron and hole, boosting the photo-to-current conversion efficiency. Under the assistance of the In_2S_3 layer, the TiO_2/$AgInS_2$ photoanode will exert much more efficiently.

Additionally, in the photoinduced i-V curves, for a semiconductor, the initial threshold bias for generating photoinduced current is similar to its flat band potential of the semiconductor material [50]. Compared with the initial threshold bias of TiO_2 NB, the initial threshold bias of TiO_2 NB/$AgInS_2$(3)/In_2S_3(7) for generating photoinduced current negatively shifts, verifying that the deposition of the $AgInS_2$(3)/In_2S_3(7) on the TiO_2 NB induces the negative shift of the flat band potential of TiO_2. Thus the deposition of $AgInS_2$/In_2S_3 on TiO_2 NB negatively pulls the band potential of TiO_2 NB caused by the more negative band of $AgInS_2$ and In_2S_3.

In Fig. 8c, the i-V curves of the TiO_2 NB, TiO_2 NB/$AgInS_2$(3), TiO_2 NB/$AgInS_2$(3)/In_2S_3(7), TiO_2 NB/In_2S_3(7) photoanodes under AM1.5 light irradiation and in the dark in the NaCl solution were also given. The photo-to-current conversion efficiency of TiO_2 NB/$AgInS_2$(3)/In_2S_3(7) which shell-core co-sensitized is much higher than that of TiO_2 NB/$AgInS_2$(3) and TiO_2 NB/In_2S_3(7) which single sensitized. The deposited In_2S_3(7) layer further dramatically enhances the generation and transfer efficiencies of photoinduced electrons, making photo-to-current conversion more effective. Besides, TiO_2 NB/$AgInS_2$(3)/In_2S_3(7) exhibits positive current over the widest bias voltage range (the whole range of − 0.8 to 1.3 V vs. Ag/AgCl), compared with TiO_2 NB/$AgInS_2$(3), TiO_2 NB/In_2S_3(7) and TiO_2 NB. Revealing that the energy band of the photoanode has been greatly pulled negatively, which will ensure the n-type semiconducting property of the photoanode even under a more negative bias voltage range [51]. This adjustment will ensure the photoanode to offer PECP current for the metals of more negative self-corrosion potentials, then facilitate the PECP for a wider variety of metals.

Figure 8d depicts the PL emission spectra of the samples. Once light irradiates the photoelectric semiconductor materials, the photogenerated electrons and holes will generate. If the photogenerated electrons and holes recombine, photoluminescence emission spectra can be used to measure the intensity of the recombination photoluminescence emission. The higher the PL emission intensity, the higher the recombination rate of the photogenerated electrons and holes. The lower the PL emission intensity, the higher the separation rate of the photogenerated electrons and holes, the higher the PEC conversion performance [52, 53]. As seen from Fig. 8d, the PL emission intensity of TiO_2 NB/$AgInS_2$(3)/In_2S_3(7) photoanode is the lowest, manifesting the lowest recombination rate of the photogenerated electrons and holes. The separation of the photogenerated electron–hole pairs in TiO_2 NB/$AgInS_2$(3)/In_2S_3(7) is more efficient than those of others. Therefore, TiO_2 NB/$AgInS_2$(3)/In_2S_3(7) possesses the maximum PEC conversion activity in corresponding to its maximum charge-separation efficiency. The multijunction structure of TiO_2 NB/$AgInS_2$(3)/In_2S_3(7) plays great importance in preventing the recombination of the electrons and holes.

The Mott–Schottky plots of the prepared composite photoanodes were adopted to establish the changes of flat band and carrier density [54], and the results are depicted in Fig. 8e. The Mott–Schottky plots of all the samples show positive slopes, manifesting the character of n-type semiconductor [55]. From the intersection point of the tangent line of Mott–Schottky curve on horizontal axis, the flat band potential of a semiconductor sample can be estimated. The flat band potential approximates to the conduction band (CB) bottom for n-type semiconductor. As seen from the Mott–Schottky plots in Fig. 8e, the flat band potentials of TiO_2 NB/$AgInS_2$(3), TiO_2 NB/$AgInS_2$(3)/In_2S_3(7) and TiO_2 NB/In_2S_3(7) are all more negative compared with that of TiO_2 NB. The flat band potential of TiO_2 NB/$AgInS_2$(3)/In_2S_3(7) is negative to − 0.63 V (vs. Ag/AgCl), i.e., − 0.43 V (vs. NHE); the flat band potential of TiO_2 NB is − 0.53 V (vs. Ag/AgCl), i.e., − 0.33 V (vs. NHE). The negative shift of the flat band potential of the photoanode is due to the deposited $AgInS_2$ and In_2S_3 with relatively negative CB potentials. The more negative flat band potential is beneficial to provide photogenerated electrons to the metal materials with negative self-corrosion potential to achieve the PECP.

Besides, the charge carrier density of samples is inversely proportional to the slope of the Mott–Schottky plots. The smaller slope indicates the larger charge carrier density [54]. From Fig. 8e, the TiO_2 NB/$AgInS_2$(3)/In_2S_3(7) exhibits a much larger charge carrier density than the TiO_2 NB, which is beneficial for the transmission of photogenerated charge carriers in the system. Thus these results indicate that the TiO_2 NB/$AgInS_2$(3)/In_2S_3(7) possesses both the more negative flat band potential and the higher charge carrier density which will benefit the superior PECP activity for metal material with more negative potential.

The impedance change of the prepared TiO_2 NB, TiO_2 NB/$AgInS_2$(3), TiO_2 NB/In_2S_3(7), TiO_2 NB/$AgInS_2$(3)/In_2S_3(7) photoanodes were examined by EIS test. Figure 8f shows the EIS Bode plots. The low frequency impedance data are usually adopted to estimate the resistance of the film (R_f) of the electrode, more precisely, the intersection of Bode plot curves on the vertical axis [56]. As seen from Fig. 8f, R_f is decreased as R_f(TiO_2 NB) > R_f(TiO_2 NB/$AgInS_2$(3)) > R_f(TiO_2 NB/In_2S_3(7)) > R_f(TiO_2 NB/$AgInS_2$(3)/In_2S_3(7)), revealing the reduce in the resistance of TiO_2 NB film after deposition of $AgInS_2$ or In_2S_3. TiO_2 NB/$AgInS_2$(3)/In_2S_3(7) exhibits a further reduced R_f compared with TiO_2 NB/$AgInS_2$(3), confirming that the In_2S_3 layer deposited around TiO_2 NB/$AgInS_2$(3) will accelerate the charge transmission and decrease the electron transmission barrier. Thus, the TiO_2 NB/$AgInS_2$(3)/In_2S_3(7) triphase junction structure will accelerate the transmission of

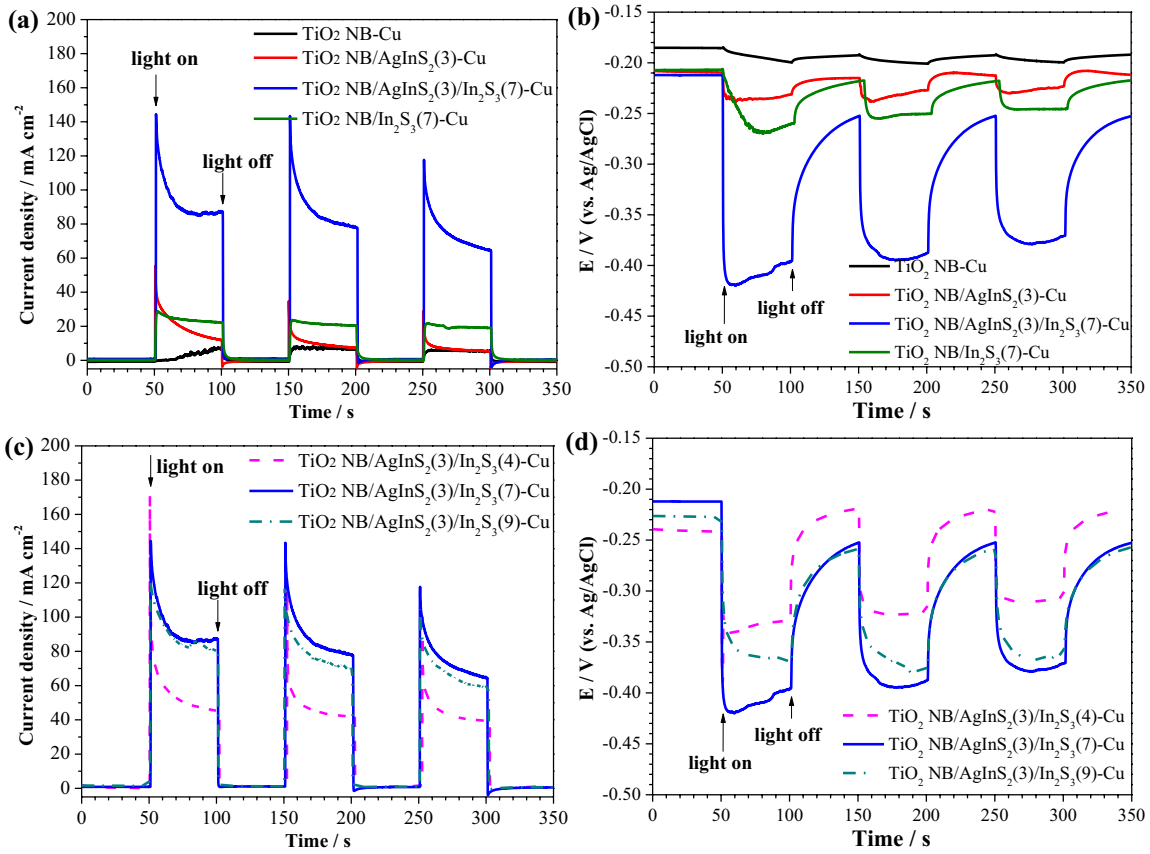

Fig. 9 The PECP current density of the fabricated photoanodes for the coupled pure copper electrode (**a**, **c**); and the photoinduced mixed potential drops of the coupling of the prepared photoanodes and the pure copper electrode (**b**, **d**) under the simulated sunlight irradiation

the photogenerated electrons under irradiation, and promote the PEC performance.

3.3 PECP performance of the fabricated film photoanodes for pure copper

The PECP performance of the TiO_2 NB, TiO_2 NB/$AgInS_2$(3), TiO_2 NB/In_2S_3(7), TiO_2 NB/$AgInS_2$(3)/In_2S_3(7) photoanodes for pure copper under simulated solar light AM1.5 irradiation in NaCl solution were measured. Figure 9a shows the PECP current densities of the photoanodes for the connected pure copper electrode. Under the simulated solar light irradiation, the current densities rise rapidly, indicating the generation of photoinduced electrons and the transfer of photoinduced electrons to the coupled pure copper electrode. The photoinduced electrons continuously accumulate on the coupled pure copper providing cathodic protection for it. The PECP current density of TiO_2 NB for the coupled pure copper is only 4.6 μA cm^{-2}, and those of TiO_2 NB/$AgInS_2$(3) and TiO_2 NB/In_2S_3(7) are 5.6 μA cm^{-2} and 20 μA cm^{-2}, respectively. The PECP current density of TiO_2 NB/$AgInS_2$(3)/In_2S_3(7) increases to 65 μA cm^{-2} which is optimum among all these photoanodes, increases more than 14 times larger than that of TiO_2 NB. Figure 9b exhibits the variation of the potential of coupling of Cu electrode and photoanodes under the simulated sunlight irradiation. It can be seen that the potentials of the connected pure copper electrode and the photoanodes negatively shift immediately with the light switched on, revealing the accumulation of photoinduced electrons on the whole coupled system. The TiO_2 NB–Cu coupling shows the photogenerated potential drop of only 15 mV. The TiO_2 NB/$AgInS_2$(3)–Cu and TiO_2 NB/In_2S_3(7)–Cu coupling show the photoinduced potential drops of 19 mV and 40 mV, respectively. The TiO_2 NB/$AgInS_2$(3)/In_2S_3(7)–Cu coupling exhibits a dramatically increased photogenerated potential drop of 160 mV. The $AgInS_2$(3)/In_2S_3(7) heterojunction deposited on TiO_2 NB greatly improve the separation of the photogenerated electron–hole pairs. Owing to the gradient matched energy bands of $AgInS_2$, In_2S_3 and TiO_2, numerous internal electric fields are built at the TiO_2/$AgInS_2$/In_2S_3 interfaces, resulting in the dramatic improvement of the separation of the photoinduced electrons and holes under simulated sunlight excitation. Simultaneously, owing to the much negative energy level potentials of $AgInS_2$ and In_2S_3, the quasi-Fermi level of the photoinduced electrons will be kept at a much

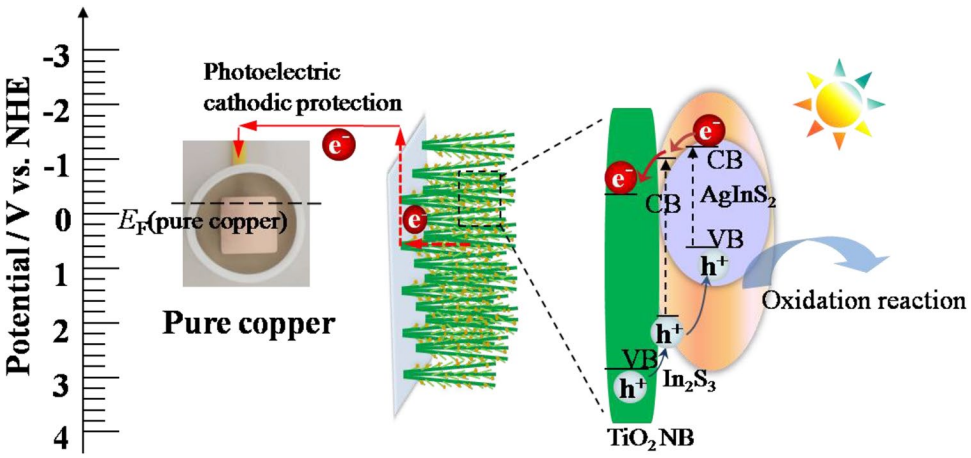

Fig. 10 The proposed schematic illustration for the enhanced PECP property of the TiO_2 NB/$AgInS_2$(3)/In_2S_3(7) photoanode under the simulated sunlight irradiation in NaCl solution

negative level, benefiting the transmission and application of photogenerated electrons to the under-protected metals with more negative self-corrosion potentials. Then, the TiO_2 NB/$AgInS_2$(3)/In_2S_3(7) photoanode offers the photoinduced electrons for Cu and achieves an excellent PECP for Cu whose self-corrosion potential is more negative (− 0.18 V vs. Ag/AgCl). Finally, the TiO_2 NB/$AgInS_2$(3)/In_2S_3(7) photoanode exhibits the highest PECP performance for Cu than others under simulated sunlight irradiation in NaCl electrolyte.

Moreover, the influence of deposition quantity on the PECP performance of TiO_2 NB/$AgInS_2$/In_2S_3 for Cu has been investigated as shown in Fig. 9c, d. Figure 9c shows the PECP current densities of the prepared TiO_2 NB/$AgInS_2$/In_2S_3 photoanode for the under-protected Cu electrode, and Fig. 9d shows the corresponding photoinduced mixed potential drops of coupling of Cu electrode and the prepared TiO_2 NB/$AgInS_2$/In_2S_3 photoanode. The different amount of $AgInS_2$ and In_2S_3 deposited on TiO_2 NB were obtained by adjusting different deposition cycles. The TiO_2 NB/$AgInS_2$(3)/In_2S_3(4)–Cu exhibits the PECP current density and the corresponding mixed potential drop of 40 μA cm^{-2} and 70 mV, respectively. TiO_2 NB/$AgInS_2$(3)/In_2S_3(9)–Cu exhibits the PECP current density and the corresponding potential drop of 60 μA cm^{-2} and 130 mV, respectively. The TiO_2 NB/$AgInS_2$(3)/In_2S_3(7)–Cu exhibits the highest PECP current and the potential drop of 65 μA cm^{-2} and 160 mV, respectively. The PECP activity of TiO_2 NB/$AgInS_2$/In_2S_3 will not reach the maximum value under less or excessive deposition of In_2S_3 assistance layer. The less In_2S_3 assistor will not sufficiently improve the PECP performance due to the insufficient formation of TiO_2 NB/$AgInS_2$/In_2S_3 multiphase junction. And the excessive In_2S_3 assistance layer will also reduce the PEC conversion due to the blocking from light harvesting and charge transport. Thus, the appropriate amount of In_2S_3 assistor is for the TiO_2 NB/$AgInS_2$(3)/In_2S_3(7) photoanode, under which the tri-phase junction in the photoanode will be fully cooperated to enhance the transmission of photogenerated electrons within interfaces. Then, the optimized construction of TiO_2 NB/$AgInS_2$(3)/In_2S_3(7) brings an superior PEC property and PECP property for Cu in NaCl solution.

3.4 Proposed mechanism for the boosted PECP property of the TiO_2 NB/$AgInS_2$/In_2S_3 photoanode

Figure 10 displays the property promotion mechanism for the boosted PEC and PECP of the TiO_2 NB/$AgInS_2$(3)/In_2S_3(7) photoanode under the simulated sunlight in NaCl solution. For the prepared TiO_2 NB/$AgInS_2$(3)/In_2S_3(7) architecture, the bandgap energy (E_g) of $AgInS_2$ is 2 eV, as deduced from the UV–Vis absorption spectra in Fig. 8b, with the CB and valence band (VB) potentials of − 1.08 and 0.82 V (vs. NHE), respectively [57]. The E_g of the In_2S_3 is 2.7 eV, as deduced from the UV–Vis absorption spectra in Fig. 8b, its CB potential is around − 0.8 V (vs. NHE) [58]. The E_g, CB and VB of TiO_2 NB are 3.2 eV, − 0.33 V and 2.87 V (vs. NHE), respectively, as deduced by the Mott–Schottky plots (Fig. 8d). Once the simulated sunlight irradiates the TiO_2 NB/$AgInS_2$(3)/In_2S_3(7), the electrons in the VBs of $AgInS_2$, In_2S_3 and TiO_2 NB will jump to their CBs and form the photogenerated electrons. Then the photogenerated electrons in the excited state continuously accumulate on the CBs, maintaining a relatively negative energy level potential. Because of the construction of gradient matched band potential among $AgInS_2$, In_2S_3 and TiO_2, their CB potentials are in the order of $E_{CB}(AgInS_2) < E_{CB}(In_2S_3) < E_{CB}(TiO_2)$, and the VB potentials of them are in the order of $E_{VB}(AgInS_2) < E_{VB}(In_2S_3) < E_{VB}(TiO_2)$. The photogenerated electrons on the CB of $AgInS_2$ will transfer to the CB of In_2S_3 then to the CB of TiO_2 for releasing energy, and the photogenerated holes on the VB of TiO_2 will transfer to the VB of In_2S_3 and to the VB of $AgInS_2$ and further react with

surroundings. Therefore, constructing $TiO_2/AgInS_2/In_2S_3$ multijunction to form numerous internal heterojunction electric fields between the phase interfaces will boost the separation and transmission of the photogenerated electrons and holes under the simulated sunlight irradiation as described in Fig. 10. Then the nanobush-like TiO_2 substrate with many ultrafine branches will provide rapid electron transmission pathway and reduce the electron transport barrier. Finally, a large amount of photogenerated electrons transfer rapidly to the coupled Cu electrode.

Additionally, owing to the negative bands of $AgInS_2$ and In_2S_3, the flat band potential of TiO_2 NB/$AgInS_2$(3)/In_2S_3(7) will be pull to a more negative value, which is also verified via the Mott–Schottky plots in Fig. 8d. Then once the simulated sunlight irradiates the photoanode, the generated and accumulated photoinduced electrons on the CB will pull the quasi-Fermi level to a negative level. For TiO_2 NB/$AgInS_2$(3)/In_2S_3(7), the large amount of the photogenerated electrons will pull the quasi-Fermi level to a more negative potential than others. Then, once couples TiO_2 NB/$AgInS_2$(3)/In_2S_3(7) with Cu electrode of a more negative self-corrosion potential, the photogenerated electrons will migrate to the Cu electrode and offer PECP for it. The TiO_2 NB/$AgInS_2$(3)/In_2S_3(7) exhibits a boosted PECP performance for Cu in NaCl electrolyte without any additional hole scavengers. This system greatly promotes the application of PEC conversion materials in cathodic protection for metals in actual marine environment. This non-toxic TiO_2NB/$AgInS_2/In_2S_3$ multijunction photoanode constructed based on the 3D nanobush architecture with both negative band potential and efficient PEC conversion performance possesses great application potential in the area of PECP under solar light irradiation.

4 Conclusions

An environmentally friendly TiO_2 NB/$AgInS_2/In_2S_3$ composite photoanode was synthesized by depositing $AgInS_2$ and In_2S_3 to the porous 3D TiO_2 nanobush architecture and form a tightly compounded multijunction structure for achieving efficient PECP. The ternary complex exerts the characteristics of each component. The $AgInS_2$ and In_2S_3 maintain the more negative band potential for TiO_2 NB which benefits the PECP for metals with negative self-corrosion potential. And the ultrafine nanobranched TiO_2 NB makes the decorated $AgInS_2$(3) and In_2S_3(7) also refined, which contributes to the reduce of the charge transfer barrier for the multijunction system. Importantly, the In_2S_3 acted as an assistor successfully constructs a gradient energy level with $AgInS_2$ sensitizer and TiO_2 NB substrate. Then, the gradient energy level among TiO_2 NB–In_2S_3–$AgInS_2$ results in the dramatically boosted PEC conversion efficiency and PECP performance for Cu whose self-corrosion potential is more negative in NaCl solution under stimulated sunlight irradiation. For TiO_2 NB/$AgInS_2$(3)/In_2S_3(7), a large number of photoinduced electrons and holes generate and transfer efficiently under simulated sunlight excitation. The ultrafined 3D framework constructed by TiO_2 NB swiftly collects the photogenerated charge carriers. The collected and accumulated large number of photoinduced electrons pulls the quasi-Fermi level to a more negative potential, assuring a more negative potential than that of Cu. Then the photogenerated electrons can transfer to the coupled Cu with a more negative self-corrosion potential and achieve an effective photogenerated cathodic protection for the coupled Cu. The photogenerated cathodic protection current density of TiO_2 NB/$AgInS_2/In_2S_3$ for Cu in NaCl solution without any hole scavengers is 70 μA cm^{-2} under the simulated sunlight excitation. This ultrafined 3D framework multijunction photoanode will help to provide strategies for the optimization of efficient photoelectric cathodic protection materials. It is helpful to realize the photoelectric cathodic protection in NaCl for more kinds of metal materials with more negative self-corrosion potential.

Acknowledgements This work was financially supported by National Natural Science Foundation of China (Grant Nos. 42176049, 41976036, 41906034), Qingdao Applied Basic Research Plan Program (Grant No. 19-6-2-79-cg), and State Key Laboratory for Marine Corrosion and Protection, Luoyang Ship Material Research Institute (LSMRI) under the Contract No. KF190408.

References

1. Xu DW, Liu Y, Zhang YH, Shi ZY, Yang MK, Zhang C, Liu B (2020) Fabrication of pyramid-$BiVO_4$/CdSe composite with controlled surface oxygen vacancies boosting efficient carriers' separation for photocathodic protection. Chem Eng J 393:10
2. Feng C, Chen Z, Jing J, Sun M, Hou J (2020) A novel TiO_2 nanotube arrays/$MgTi_xO_y$ multiphase-heterojunction film with high efficiency for photoelectrochemical cathodic protection. Corros Sci 166:108441
3. Wang X, Guan ZC, Jin P, Tang YY, Song GL, Liu GK, Du RG (2019) Facile fabrication of $BiVO_4$ modified TiO_2 nanotube film photoanode and its photocathodic protection effect on stainless steel. Corros Sci 157:247–255
4. Yang Y, Cheng W, Cheng YF (2019) Preparation of Co_3O_4@ZnO core–shell nanocomposites with intrinsic p–n junction as high-performance photoelectrodes for photoelectrochemical cathodic protection under visible light. Appl Surf Sci 476:815–821
5. Ding D, Hou QK, Su YG, Li QQ, Liu L, Jing J, Lin B, Chen Y (2019) g-C_3N_4/TiO_2 hybrid film on the metal surface, a cheap and efficient sunlight active photoelectrochemical anticorrosion coating. J Mater Sci Mater Electron 30:12710–12717
6. Liang D, Huang Y, Wu F, Luo J, Yi X, Wang J, Qiu X (2019) In situ synthesis of g-C_3N_4/TiO_2 with 001 and 101 facets coexposed for water remediation. Appl Surf Sci 487:322–334
7. Bao Z, Fu N, Qin Y, Lv J, Wang Y, He J, Hou Y, Jiao C, Chen D, Wu Y, Dai JY (2019) Broadband plasmonic enhancement of high-efficiency dye-sensitized solar cells by incorporating Au@

Ag@SiO_2 core–shell nanocuboids. ACS Appl Mater Interfaces 12:538–545
8. Peng C, Wei P, Li X, Liu Y, Cao Y, Wang H, Yu H, Peng F, Zhang L, Zhang B, Lv K (2018) High efficiency photocatalytic hydrogen production over ternary Cu/TiO_2@$Ti_3C_2T_x$ enabled by low-work-function 2D titanium carbide. Nano Energy 53:97–107
9. Sharif T, Ghayeb Y, Mohammadi T, Momeni MM, Bagheri R, Song Z (2021) Surface treatment of titanium by in-situ anodization and NiO photodeposition: enhancement of photoelectrochemical properties for water splitting and photocathodic protection of stainless steel. Appl Phys A 127:72
10. Momeni MM, Motalebian M (2021) Chromium-doped titanium oxide nanotubes grown via one-step anodization for efficient photocathodic protection of stainless steel. Surf Coat Technol 420:127304
11. Momeni MM, Taghinejad M, Ghayeb Y, Bagheri R, Song Z (2020) High-efficiency photoelectrochemical cathodic protection performance of the iron-nitrogen-sulfur-doped TiO_2 nanotube as new efficient photoanodes. Mater Res Express 7:086403
12. Momeni MM, Motalebian M, Ghayeb Y, Atapour M (2021) Photoelectrochemical cathodic protection of stainless steel using W- and Cr-doped/codoped TiO_2 nanotube thin film photoanodes. J Electrochem Soc 168:081504
13. Momeni MM, Zeinali P (2021) Fabrication of Ag electrodeposited-iron doped TiO_2 nanotube composites for photoelectrochemical cathodic protection applications. J Electroanal Chem 891:115283
14. Momeni MM, Ghayeb Y, Moosavi N (2018) Preparation of Ni–Pt/Fe–TiO_2 nanotube films for photoelectrochemical cathodic protection of 403 stainless steel. Nanotechnology 29:425701
15. Momeni MM, Ghayeb Y, Akbarnia M, Barati Z (2020) Successive ionic layer adsorption and reaction (SILAR) deposition of nickel sulfide on the Fe_2O_3 nanotube for efficient photocathodic protection of stainless steel under visible light. J Iran Chem Soc 17:3367–3374
16. Momeni MM, Mahvari M, Ghayeb Y (2019) Photoelectrochemical properties of iron–cobalt WTiO_2 nanotube photoanodes for water splitting and photocathodic protection of stainless steel. J Electroanal Chem 832:7–23
17. Momeni MM, Zeinali P (2021) Photochemical deposition of Ag, Cu, Cu@Ag, and Ag@Cu on TiO_2 nanotubes and their optical properties and photoelectrochemical activity. J Electron Mater 50:5810–5818
18. Fu N, Jiang X, Chen D, Duan Y, Zhang G, Chang M, Fang Y, Lin Y (2019) Au/TiO_2 nanotube array based multi-hierarchical architecture for highly efficient dye-sensitized solar cells. J Power Sources 439:227076
19. Xie H, Li N, Chen X, Jiang J, Zhao X (2020) Surface oxygen vacancies promoted photodegradation of benzene on TiO_2 film. Appl Surf Sci 511:145597(1–9)
20. Liu Q, Wu Y, Zhang J, Chen K, Huang C, Chen H, Qiu X (2019) Plasmonic MoO_{3-x} nanosheets with tunable oxygen vacancies as efficient visible light responsive photocatalyst. Appl Surf Sci 490:395–402
21. Dong F, Wang H, Sen G, Wu Z, Lee SC (2011) Enhanced visible light photocatalytic activity of novel Pt/C-doped TiO_2/$PtCl_4$ three-component nanojunction system for degradation of toluene in air. J Hazard Mater 187:509–516
22. Liu FS, Wang S, Liu LL, Du H (2012) Preparation and photocatalysis property of P–N coupled photocatalyst CoO/CdS/TiO_2. Adv Mater Res 512–515:1677–1682
23. Cotal H, Fetzer C, Boisvert J, Kinsey G, King R, Hebert P, Yoon H, Karam N (2009) III–V multijunction solar cells for concentrating photovoltaics. Energy Environ Sci 2:174–192
24. King RR, Law DC, Edmondson KM, Fetzer CM, Kinsey GS, Yoon H, Sherif RA, Karam NH (2007) 40% efficient metamorphic GaInP/GaInAs/Ge multijunction solar cells. Appl Phys Lett 90:510
25. Dai L, Du X, Jiang D, Chen W, Zhu M, Wang K (2017) Ultrafine alpha-Fe_2O_3 nanocrystals anchored on N-doped graphene: a nanomaterial with long hole diffusion length and efficient visible light-excited charge separation for use in photoelectrochemical sensing. Microchim Acta 184:137–145
26. Xu YF, Wang XD, Chen HY, Kuang DB, Su CY (2016) Toward high performance photoelectrochemical water oxidation: combined effects of ultrafine cobalt iron oxide nanoparticle. Adv Funct Mater 26:4414–4421
27. Wang J, Wang M, Zhang T, Wang Z, Guo P, Su J, Guo L (2018) Facile synthesis of ultrafine hematite nanowire arrays in mixed water-ethanol-acetic acid solution for enhanced charge transport and separation. ACS Appl Mater Interfaces 10:12594–12602
28. Wang D, Liu Y, Yu B, Zhou F, Liu W (2009) TiO_2 nanotubes with tunable morphology, diameter, and length: synthesis and photoelectrical/catalytic performance. Chem Mater 21:1198–1206
29. Chang WS, Wu CC, Jeng MS, Cheng KW, Huang CM, Lee TC (2010) Ternary Ag–In–S polycrystalline films deposited using chemical bath deposition for photoelectrochemical applications. Mater Chem Phys 120:307–312
30. Choi Y, Seol M, Kim W, Yong K (2014) Chemical bath deposition of stoichiometric CdSe quantum dots for efficient quantum-dot-sensitized solar cell application. J Phys Chem C 118:5664–5670
31. Sun M, Chen Z, Li J, Hou J, Xu F, Xu L, Zeng R (2018) Enhanced visible light-driven activity of TiO_2 nanotube array photoanode co-sensitized by "green" $AgInS_2$ photosensitizer and In_2S_3 buffer layer. Electrochim Acta 269:429–440
32. Jiang X, Sun M, Chen Z, Jing J, Feng C (2020) High-efficiency photoelectrochemical cathodic protection performance of the TiO_2/$AgInSe_2$/In_2Se_3 multijunction nanosheet array. Corros Sci 176:108901
33. Jiang X, Sun M, Chen Z, Jing J, Feng C (2020) An ultrafine hyperbranched CdS/TiO_2 nanolawn photoanode with highly efficient photoelectrochemical performance. J Alloys Compd 816:152533
34. Sun WT, Yu Y, Pan HY, Gao XF, Chen Q, Peng LM (2008) CdS quantum dots sensitized TiO_2 nanotube-array photoelectrodes. J Am Chem Soc 130:1124–1125
35. Cui X, Gu H, Guan Y, Ren G, Ma Z, Yin Y, Liu J, Cui X, Yao L, Yin Y (2015) Fabrication of $AgInS_2$ nanoparticles sensitized TiO_2 nanotube arrays and their photoelectrochemical properties. Sol Energy Mater Sol Cells 137:101–106
36. Peng S, Zhang S, Mhaisalkar SG, Ramakrishna S (2012) Synthesis of $AgInS_2$ nanocrystal ink and its photoelectrical application. Phys Chem Chem Phys 14:8523–8529
37. Liu B, Li X, Zhao Q, Ke J, Tadé M, Liu S (2016) Preparation of $AgInS_2$/TiO_2 composites for enhanced photocatalytic degradation of gaseous o-dichlorobenzene under visible light. Appl Catal B 185:1–10
38. Kang HP, Jang K, Son SU (2010) Synthesis, optical properties, and self-assembly of ultrathin hexagonal In_2S_3 nanoplates. Angew Chem Int Ed 45:4608–4612
39. He Y, Li D, Xiao G, Chen W, Chen Y (2009) A new application of nanocrystal In_2S_3 in efficient degradation of organic pollutants under visible light irradiation. J Phys Chem C 113:5254–5262
40. Bhat SSM, Pawar SA, Potphode D, Moon C-K, Suh JM, Kim C, Choi S, Patil DS, Kim J-J, Shin JC, Jang HW (2019) Substantially enhanced photoelectrochemical performance of TiO_2 nanorods/CdS nanocrystals heterojunction photoanode decorated with MoS_2 nanosheets. Appl Catal B 259:118102
41. Anwar M, Hogarth CA, Bulpett R (1990) An XPS study of amorphous MoO_3/SiO films deposited by co-evaporation. J Mater Sci 25:1784–1788

42. Andrulevičius M, Tamulevičius S, Gnatyuk Y, Vityuk N, Smirnova N, Eremenko A (2008) XPS investigation of $TiO_2/ZrO_2/SiO_2$ films modified with Ag/Au nanoparticles. Mater Sci 14:8–14
43. Guo Y, Ao Y, Wang P, Wang C (2019) Mediator-free direct dual-Z-scheme $Bi_2S_3/BiVO_4/MgIn_2S_4$ composite photocatalysts with enhanced visible-light-driven performance towards carbamazepine degradation. Appl Catal B 254:479–490
44. Tan L, Liu S, Li X, Chronakis IS, Shen Y (2015) A new strategy for synthesizing $AgInS_2$ quantum dots emitting brightly in near-infrared window for in vivo imaging. Colloids Surf B 125:222–229
45. Xiang W, Xie C, Wang J, Zhong J, Liang X, Yang H, Luo L, Chen Z (2014) Studies on highly luminescent $AgInS_2$ and Ag–Zn–In–S quantum dots. J Alloys Compd 588:114–121
46. Liu B, Hu X, Li X, Li Y, Chen C, Lam K-h (2017) Preparation of $ZnS@In_2S_3$ core@shell composite for enhanced photocatalytic degradation of gaseous o-dichlorobenzene under visible light. Sci Rep 7:16396
47. Hong KJ, Jeong JW, Jeong TS, Youn CJ, Lee WS, Park JS, Shin DC (2003) Photocurrent study of the valence band splitting of $AgInS_2$ epilayers on GaAs. J Phys Chem Solids 64:1119–1124
48. Ortega-López M, Vigil-Galán O, Gandarilla FC, Solorza-Feria O (2003) Preparation of $AgInS_2$ chalcopyrite thin films by chemical spray pyrolysis. Mater Res Bull 38:55–61
49. Shay JL, Tell B, Schiavone LM, Kasper HM, Thiel F (1974) Energy bands of $AgInS_2$ in the chalcopyrite and orthorhombic structures. Phys Rev B 9:1719–1723
50. Gstrein F (2004) Electron-transfer processes at semiconductor/liquid interfaces and metal/nanogap junctions. California Institute of Technology, Pasadena
51. Jing J, Chen Z, Feng C (2021) Using the photoinduced voltampere curves to study the p/n types of the corrosion products with semiconducting properties. J Electroanal Chem 881:114961
52. Zhou X, Jin B, Li L, Peng F, Wang H, Yu H, Fang Y (2012) A carbon nitride/TiO_2 nanotube array heterojunction visible-light photocatalyst: synthesis, characterization, and photoelectrochemical properties. J Mater Chem 22:17900–17905
53. Chen Y, Huang W, He D, Yue S, Huang H (2014) Construction of heterostructured g-C_3N_4/Ag/TiO_2 microspheres with enhanced photocatalysis performance under visible-light irradiation. ACS Appl Mater Interfaces 6:14405–14414
54. Jing JP, Chen ZY, Bu YY, Sun MM, Zheng WQ, Li WB (2019) Significantly enhanced photoelectrochemical cathodic protection performance of hydrogen treated Cr-doped $SrTiO_3$ by Cr^{6+} reduction and oxygen vacancy modification. Electrochim Acta 304:386–395
55. Gelderman K, Lee L, Donne SW (2007) Flat-band potential of a semiconductor: using the Mott Schottky equation. J Chem Educ 84:685–688
56. Sun M, Chen Z, Jiang X, Feng C, Zeng R (2018) Optimized preparation of Co–Pi decorated g-C_3N_4@ZnO shell–core nanorod array for its improved photoelectrochemical performance and stability. J Alloys Compd 780:540–551
57. Zhang W, Li D, Chen Z, Sun M, Li W, Lin Q, Fu X (2011) Microwave hydrothermal synthesis of $AgInS_2$ with visible light photocatalytic activity. Mater Res Bull 46:975–982
58. Xu Y, Schoonen MAA (2000) The absolute energy positions of conduction and valence bands of selected semiconducting minerals. Am Mineral 85:543–556

Publisher's Note Springer Nature remains neutral with regard to jurisdictional claims in published maps and institutional affiliations.

Authors and Affiliations

Mengmeng Sun[1,3,4] · Zhuoyuan Chen[2] · Xuhong Jiang[1,3,4,5] · Guiying Lu[1,3,4,5] · Jiangping Jing[2] · Chang Feng[2]

[1] Key Laboratory of Marine Environmental Corrosion and Bio-fouling, Institute of Oceanology, Chinese Academy of Sciences, 7 Nanhai Road, Qingdao 266071, China

[2] School of Materials Science and Hydrogen Energy, Foshan University, 18 Jiangwanyi Road, Foshan 528000, China

[3] Open Studio for Marine Corrosion and Protection, Pilot National Laboratory for Marine Science and Technology (Qingdao), No. 1 Wenhai Road, Qingdao 266237, China

[4] Center for Ocean Mega-Science, Chinese Academy of Sciences, 7 Nanhai Road, Qingdao 266071, China

[5] University of Chinese Academy of Sciences, 19 (Jia) Yuquan Road, Beijing 100049, China